The Astrophysical Journal Letters, 836:L9 (6pp), 2017 February 10 https://doi.org/10.3847/2041-8213/aa5c7e

SNe Ia Keep Memory of Their Progenitor Metallicity

Luciano Piersanti[1,2], Eduardo Bravo[3], Sergio Cristallo[1,2], Inmaculada Domínguez[4], Oscar Straniero[1,5], Amedeo Tornambé[6], and Gabriel Martínez-Pinedo[7,8]
[1] INAF-Osservatorio Astronomico di Teramo, via Mentore Maggini, snc, I-64100, Teramo, Italy; piersanti@oa-teramo.inaf.it
[2] INFN-Sezione di Perugia, via Pascoli, Perugia, Italy; cristallo@oa-teramo.inaf.it
[3] E.T.S. Arquitectura del Vallés, Universitat Politècnica de Catalunya, Carrer Pere Serra 1-15, E-08173 Sant Cugat del Vallès, Spain; eduardo.bravo@upc.es
[4] Universidad de Granada, E-18071 Granada, Spain; inma@ugr.es
[5] INFN, Laboratori Nazionali del Gran Sasso (LNGS), I-67100 Assergi, Italy; straniero@oa-teramo.inaf.it
[6] INAF-Osservatorio Astronomico di Roma, via Frascati, 33, I-00040, Monte Porzio Catone, Italy; tornambe@oa-roma.inaf.it
[7] GSI Helmholtzzentrum für Schwerioneneforschung, Planckstraße 1, D-64291 Darmstadt, Germany; g.martinez@gsi.de
[8] Institut für Kernphysik (Theoriezentrum), Technische Universität Darmstadt, Schlossgartenstraße 2, D-64289 Darmstadt, Germany
Received 2016 December 16; accepted 2017 January 26; published 2017 February 9

Abstract

The ultimate understanding of SNe Ia diversity is one of the most urgent issues to exploit thermonuclear explosions of accreted White Dwarfs (WDs) as cosmological yardsticks. In particular, we investigate the impact of the progenitor system metallicity on the physical and chemical properties of the WD at the explosion epoch. We analyze the evolution of CO WDs through the accretion and simmering phases by using evolutionary models based on time-dependent convective mixing and an extended nuclear network including the most important electron captures, beta decays, and URCA processes. We find that, due to URCA processes and electron-captures, the neutron excess and density at which the thermal runaway occurs are substantially larger than previously claimed. Moreover, we find that the higher the progenitor metallicity, the larger the neutron excess variation during the accretion and simmering phases and the higher the central density and the convective velocity at the explosion. Hence, the simmering phase acts as an amplifier of the differences existing in SNe Ia progenitors. When applying our results to the neutron excess estimated for the Tycho and *Kepler* young supernova remnants, we derive that the metallicity of the progenitors should be in the range $Z = 0.030$–0.032, close to the average metallicity value of the thin disk of the Milky Way. As the amount of ^{56}Ni produced in the explosion depends on the neutron excess and central density at the thermal runaway, our results suggest that the light curve properties depend on the progenitor metallicity.

Key words: accretion, accretion disks – nuclear reactions, nucleosynthesis, abundances – supernovae: general – supernovae: individual (Tycho, *Kepler*)

1. Introduction

Nowadays it is largely accepted that supernovae Ia (SNe Ia) are produced by the thermonuclear disruption of CO white dwarfs (WDs) accreting matter from their companions in binary systems (Hoyle & Fowler 1960). In fact, the growth in mass of the degenerate object determines its compressional heating. For intermediate values of the accretion rate ($10^{-8} \leqslant \dot{M} \leqslant 10^{-7}\,M_{\odot}\,\mathrm{yr}^{-1}$) when the accreting WD approaches the Chandrasekhar mass limit, C-ignition occurs at the center where the effects of compressional heating are larger (e.g., see Piersanti et al. 2003). The energy delivered by C-burning increases the local temperature and, hence, the burning rate speeds up. The large energy excess can not be transferred radiatively, so the WD inner zones become unstable for convection. As C-burning proceeds, the convective zone extends outwards in mass, while temperature in the inner zones continues to increase, until it attains $\sim 8 \times 10^8$ K and the explosion occurs (Wunsch & Woosley 2004). The time from the onset of convection to explosion lasts several 10^4 year and it is usually called *simmering phase*.

The accretion and simmering phases determine the WD properties at the explosion. In particular, the energy and chemical composition of the ejecta are determined by the thermonuclear flame propagation whose properties depend on the thermal and turbulent state of the WD (Nomoto et al. 1984; Woosley & Weaver 1986). Moreover, the dimension and distribution of ignition points at the explosion depend on the temperature fluctuations already present in the convective core of the exploding WD (García-Senz & Woosley 1995; Wunsch & Woosley 2004). Finally, the pre-explosive evolution fixes the WD neutron excess η, thus determining the amount of ^{56}Ni produced during the explosion and, hence, the luminosity at maximum of SNe Ia (Timmes et al. 2003; Bravo et al. 2010). All these effects are thought to contribute to the SNe Ia homogeneity, by erasing the identity hallmarks of the exploding WD progenitor (the so-called "stellar amnesia"—Höflich et al. 2003). However, such an amnesia cannot be global, as suggested by the correlation observed between SNe Ia luminosity and metallicity of their environment (e.g., Moreno-Raya et al. 2016).

As mass is transferred, the WD contracts and density increases. When the electron Fermi energy becomes large enough, electron-capture processes occur. The capture threshold is typically lower for odd-mass nuclei due to odd–even effects in the nuclear masses. Electron-capture is followed by the beta-decay of the daughter nucleus producing an URCA process, in which electron-capture on the isobar with charge Z alternates with the beta-decay of the $(Z-1)$ isobar. During this process, the abundances are not changed, but due to the ν_e and $\bar{\nu}_e$ emission substantial cooling occurs (Tsuruta & Cameron 1970). The cooling efficiency is larger at the so-called URCA density, ρ_{URCA} for which electron-capture and beta-decay processes operate with the same rate. Increasing

density, electron-capture on even-mass nuclei becomes possible. Due to pairing effects, the capture threshold for a second electron-capture on the produced odd–odd nucleus is much lower than for the first capture in the even–even nucleus. Hence, there is no URCA process but a double electron-capture that heats as the second capture populates final states at high excitation energy decaying by gamma emission. We denote ρ_{2EC} the density at which the electron Fermi energy becomes equal to the threshold for the first capture. In stellar environment URCA processes in odd-mass nuclei and double electron-capture in even-mass nuclei operate simultaneously. Typically, URCA processes dominate the temperature evolution, as they operate for several cycles, and double electron-captures the neutronization, as even-mass nuclei are more abundant.

Paczyński (1972) recognized early that URCA processes could play an important role during the simmering phase. In the WD regions where the density is close to ρ_{URCA}, the so-called URCA shell, both nuclides participating in URCA processes have similar abundances. The continuous density increase in the accreting WD causes the URCA shell to move outward in mass, and the region interior to the URCA shell becomes enriched in the proton-poor isobar, $^{A}(Z-1)$, i.e., it becomes neutronized. Similarly, for even A nuclei the transition from regions enriched in the $^{A}(Z-2)$ isobar to those enriched in the ^{A}Z isobar occurs at densities close to ρ_{2EC}. During the accretion phase URCA processes and double electron-captures operate locally. After C-ignition, when convection sets in, convective URCA and double electron-captures followed by double-beta decays occur. If the proton-poor isobar of an URCA pair or double electron-capture triplet is transported by convective eddies across the URCA shell to lower densities, it beta-decays to the proton-rich isobar. Afterward, the convective eddies move the latter once more to the high-density regions of the WD and electron-capture occurs. In this process, the global abundances are not changed and there is no net neutronization, but, due to ν_e and $\bar{\nu}_e$ emission, a substantial cooling occur. During the explosion, the inner $\sim 0.2\ M_{\odot}$ of the WD are incinerated, and neutronized to values in excess of those found at the end of the simmering phase.

In the past many works were devoted to explore the effect of URCA processes during the simmering phase (Bruenn 1973; Couch & Arnett 1975; Iben 1978a, 1978b, 1982; Barkat & Wheeler 1990; Mochkovitch 1996; Stein et al. 1999; Bisnovatyi-Kogan 2001; Lesaffre et al. 2005). Denissenkov et al. (2015) included URCA processes in the evolution of accreting CO WDs and showed that they affects the physical properties at the C-ignition epoch and, hence, the density at the explosion. Piro & Bildsten (2008) derived η at the explosion using a semi-analytical model for the ^{12}C consumption during the simmering phase. They did not address the effects of URCA processes and derived the neutronization independently of the progenitor metallicity. A similar evaluation was performed by Chamulak et al. (2008) by means of one-zone model coupled to a nuclear network. More recently, Martínez-Rodríguez et al. (2016) performed the first consistent evaluation of the neutron excess at the explosion epoch. They computed evolutionary model of WDs from the accretion phase up to the explosion by considering explicitly the ^{23}(Na, Ne) and ^{25}(Mg, Na) URCA pairs. The final neutronization they derived is dominated by convective URCA processes and only mildly dependent on the progenitor metallicity. All these works obtained a small increase of the central neutronization during the simmering phase ($0.3 \times 10^{-3} - 10^{-3}$), definitively too low to explain the neutron excess in the exploding WD as estimated for the Supernova remnants in the thin disk of the Galaxy (Badenes et al. 2008; Park et al. 2013).

In this work we investigate the dependence of the physical properties and neutronization at the explosion on the accretion and simmering phases. To this aim we consider WD progenitors with different initial metallicities and we adopt an extended nuclear network. In Section 2 we present the initial CO WD models and illustrate the computational method; in Section 3 we present our results; in Section 4 we summarize our conclusions.

2. Initial Models and Assumptions

We assume the Double Degenerate scenario for SNe Ia progenitors (Iben & Tutukov 1984) and we consider three different initial binary systems, namely $(M_1, M_2) = (3.2, 1.5)$, (4.5, 1.8) and (5.3, 2.0) $M_{\odot}$ having initial chemical composition $(Y, Z) = (0.245, 2.45 \times 10^{-4})$ (model ZLOW), $(0.269, 1.38 \times 10^{-2})$ (model ZSUN), and $(0.305, 4 \times 10^{-2})$ (model ZHIG), respectively. Heavy elements in ZSUN and ZHIG models have a scaled-solar abundances, while for the ZLOW model we assume $[Fe/H] = -2$ and $[\alpha/H] = 0.5$.[9] Computations have been performed with the FUNS code (Straniero et al. 2006; Cristallo et al. 2009), from the pre-main sequence phase up to the tip of the AGB. The primary component of each binary system evolves into a CO WD with total mass $M_{WD} = 0.817\ M_{\odot}$, while the secondary evolves into a $\sim 0.6\ M_{\odot}$ CO WD, the exact mass value depending on the considered case. The more massive WDs are evolved along the cooling sequence for $\simeq 1$ Gyr, until the models attain the following physical conditions: $L_{sup} = 1.76 \times 10^{-3}\ L_{\odot}$, $T_{eff} = 1.20 \times 10^{4}\ K$, $T_C = 1.1 \times 10^{7}$ K and $\rho_C = 1.22 \times 10^{7}$ g cm^{-3}. Due to gravitational wave radiation, the secondary WD undergoes a dynamical mass transfer via Roche lobe overflow, disrupting in a massive accretion disk around the primary WD. Hence, we assume that matter is transferred from the disk at $\dot{M} = 10^{-7}\ M_{\odot}$ yr^{-1}. The chemical composition of the accreted matter is fixed by assuming that during the dynamical mass transfer the material of the original secondary WD is fully mixed.

To describe properly the evolution of accreted WDs through the simmering phase and up to the explosion, the FUN code solves simultaneously the equations describing the evolution of the stellar physical structure and those describing the evolution of chemicals, as determined by both nuclear burning and convective mixing. In convective zones we model the mixing as an advective process, adopting as advection velocity the values computed according to the mixing length theory of convection (Cox & Giuli 1968). In our computations we use a large nuclear network including 300 processes and 81 isotopes, namely: n, p, α, C (12–14), N (13–15), O (16–19), F (18–21), Ne (20,23), Na (22–25), Mg (23,27), Al (25–28), Si (27–32), P (30–33), S (31–37), Cl (35–38), Ar (36–42), K (38–43), Ca (40–46), SC (45–46), ^{56}Cr, ^{56}Mn, and ^{56}Fe. The URCA processes we consider are listed in Table 1. Rates provided by Oda et al. (1994) are interpolated by adopting the Fuller et al. (1985) effective formalism. The rates for ^{56}Fe–^{56}Mn–^{56}Cr have been recomputed in a fine density and temperature grid based

[9] We adopt the heavy elements distribution provided by Lodders (2003) so that $Z_{\odot} = 1.38 \times 10^{-2}$ (see Piersanti et al. 2007).

Table 1
URCA Pairs (Lines 1–8) and Double Electron-capture Triplets (Lines 9–10) Considered in the Present Work

Isobars	$\rho_{\rm URCA}$ or $\rho_{\rm 2EC}$ in 10^9 g cm^{-3}	$X_\odot$ [a]	Source
^{19}F–^{19}O	2.43	1.07×10^{-7}	Suzu2016
^{21}Ne–^{21}F	3.78	3.74×10^{-5}	Suzu2016
^{23}Na–^{23}Ne	1.86	1.42×10^{-4}	Suzu2016
^{25}Mg–^{25}Na	1.31	3.84×10^{-5}	Suzu2016
^{27}Al–^{27}Mg	0.104	5.60×10^{-5}	Suzu2016
^{31}P–^{31}Si	1.09	6.68×10^{-6}	Oda1994
^{37}Cl–^{37}S	2.19	3.03×10^{-6}	Oda1994
^{39}K–^{39}Ar	0.012	3.39×10^{-6}	Oda1994
^{32}S–^{32}P–^{32}Si	0.144	3.14×10^{-4}	Oda1994
^{56}Fe–^{56}Mn–^{56}Cr	1.27	1.05×10^{-3}	Lang2001

Note. Suzu2016 : Suzuki et al. (2016), Oda1994 : Oda et al. (1994), Lang2001: Langanke & Martínez-Pinedo (2001).
[a] Mass fraction abundance of the β-stable isotope in the initial ZSUN model.

on the same input used in Langanke & Martínez-Pinedo (2001). The ^{13}N$(e^-, \nu_e)^{13}$C rate is computed using the experimental data provided by Zegers et al. (2008). The ^{12}C+^{12}C reaction rate is taken from Caughlan & Fowler (1988). We assume that the explosion of the accreted WD occurs when the maximum temperature attains $T_{\rm exp} = 8 \times 10^8$ K, i.e., when the nuclear heating timescale approaches the turnover timescale of the convective region (Wunsch & Woosley 2004).

3. Results

The compression of the accreting WD via mass deposition determines the homologous increase of density, while the evolution of the temperature profile is determined by the exact value adopted for $\dot{M}$ (e.g., see Piersanti et al. 2003). For intermediate values of $\dot{M}$, as the one adopted in this work, initially the gravitational energy released on the surface of the accreting WD causes the local increase of temperature. When the evolutionary time becomes comparable to the thermal diffusion timescale, the temperature at the center increases. Later on and up to the C-ignition epoch, the temperature evolution is determined by the homologous compression. This is clearly illustrated in the upper panel of Figure 1, where we report the evolution of the center of the ZSUN model (solid line).

As density increases, electron-captures on some nuclei become active. This affects the further evolution and, hence, the neutronization of the whole WD at the explosion in two different ways. In fact, electron-captures increase the local neutronization in the innermost zone of the accreting WD so that the final neutronization at the explosion is larger. Moreover, due to the neutrino emission associated with electron-capture and beta-decay, the local temperature is reduced. Hence, a larger amount of mass has to be accreted to attain C-ignition, which will occur at larger density and lower temperature. This occurrence affects the simmering phase, determining a larger final neutronization at the explosion, as illustrated in the lower panel of Figure 1, depicting the evolution of central η of the ZSUN model (solid line). To disentangle the URCA processes effects, we compute two additional models, by excluding from the nuclear network

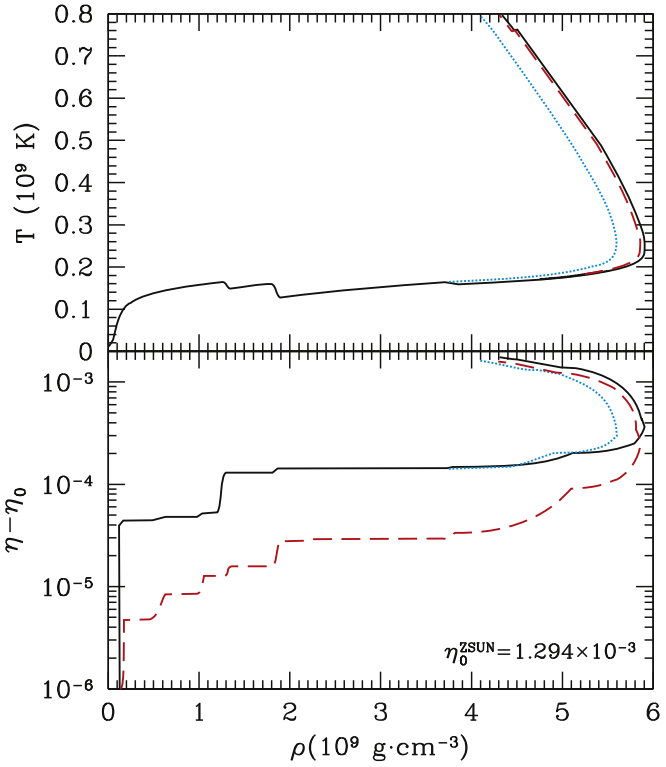

Figure 1. Upper panel: evolution in the $\rho - T$ plane of the center of the model ZSUN (solid line). Lower panel: evolution of the neutronization variation at the center $\Delta\eta = \eta(t) - \eta_0$ as a function of the central density (solid line). Dashed and dotted lines refer to the NoSFe and NoNe21 models, respectively.

some URCA processes. When the ^{32}(S, P, Si) and ^{56}(Fe, Mn, Cr) URCA triplets are excluded (model NoSFe in Table 2—dashed lines in Figure 1), the WD energy budget is only slightly altered, so that the physical conditions at the C-ignition and explosion epochs do not change appreciably. The final neutronization is $\Delta\eta \simeq 0.11 \times 10^{-3}$ lower, corresponding to the ^{56}Fe and ^{32}S contribution already present in the initial WD. The exclusion of the ^{21}(Ne, F) URCA pair from the nuclear network (model NoNe21 in Table 2—dotted lines in Figure 1) produces a small effect on the central neutronization before C-ignition ($\Delta\eta \simeq 4 \times 10^{-6}$—see lower panel in Figure 1), while the central temperature is about 5% larger. Hence, in model NoNe21 C-ignition occurs sooner and at lower density (see Table 2) and during the whole simmering phase up to the explosion the density profile remains lower than in the model ZSUN. This causes the neutronization at the explosion to be smaller by $\Delta\eta \simeq 4 \times 10^{-5}$, an order of magnitude larger than the difference before C-ignition.

The neutron excess before C-ignition is affected also by electron-captures on several isotopes such as ^{41}K, which has an activation density of $\rho_{\rm ec} = 9.12 \times 10^8$ g cm^{-3} and mass fraction abundance $X_\odot(^{41}{\rm K}) = 8.18 \times 10^{-7}$. An interesting case is the electron-capture on ^{36}Ar (initial abundance $X_\odot$ (^{36}Ar) $= 6.74 \times 10^{-5}$ and $\rho_{\rm ec} = 1.71 \times 10^8$ g cm^{-3}), producing ^{36}Cl . However, when the local density increases above 5.76×10^8 g cm^{-3} due to the continuous mass deposition, the ^{36}Cl$(e^-, \nu_e)^{36}$S process occurs.

Figure 2 illustrates the interplay between heating, as determined by homologous compression, and cooling, due to URCA processes. When central density exceeds $\rho_{\rm URCA}$ for a given URCA pair, the center is cooled; as matter continues to

Table 2
Model Inputs and Results

Model	ZLOW	ZSUN	ZHIG	NoSFe	NoNe21
$M_{\rm MS}$ ($M_\odot$)	3.2	4.5	5.3	4.5	4.5
$Z_{\rm ini}$ (10^{-3})	0.245	13.80	40.00	13.80	13.80
$M_{\rm acc}$ ($M_\odot$)	0.566	0.567	0.564	0.567	0.566
$t_{\rm acc}$ (10^6 year)	5.663	5.671	5.639	5.669	5.662
$t_{\rm simm}$ (10^4 year)	2.872	2.822	3.461	2.794	2.846
$\rho_{\rm ign}$ (10^9g cm^{-3})	3.727	4.509	5.305	4.519	4.350
$T_{\rm ign}$ (10^8 K)	1.947	1.671	1.494	1.683	1.729
$\rho_{\rm simm}$ (10^9g cm^{-3})	4.042	5.113	6.250	5.085	4.883
$T_{\rm simm}$ (10^8 K)	2.023	1.778	1.624	1.786	1.831
$M(^{12}{\rm C})_{\rm ini}$ ($M_\odot$)	0.562	0.548	0.503	0.548	0.548
$M(^{12}{\rm C})_{\rm fin}$ ($M_\odot$)	0.536	0.521	0.468	0.521	0.510
$\Delta M(^{12}{\rm C})(10^{-2}M_\odot)$	2.620	2.763	3.585	2.732	2.779
$M^{\rm max}_{\rm conv}$ ($M_\odot$)	1.267	1.239	1.217	1.235	1.238
$M_{\rm exp}$ (10^{-2} $M_\odot$)	0.000	0.000	1.486	0.000	0.000
$\rho_{\rm exp}$ (10^9g cm^{-3})	3.374	4.299	5.073	4.287	4.068
$\eta_{\rm exp}$ (10^{-3})	1.149	2.996	6.478	2.884	2.924
$v_{\rm exp}$ (km s^{-1})	554	713	863	710	672
$\overline{\eta}_{\rm exp}$ (10^{-3})	0.668	2.368	5.472	2.262	2.308
$\eta_{\rm c,0}$ (10^{-3})	0.022	1.294	3.752	1.294	1.294

Note. $M_{\rm MS}$: progenitor mass in the main sequence phase; $M_{\rm acc}$: total accreted mass; $t_{\rm acc}$: time from the onset of mass transfer up to the explosion; $t_{\rm simm}$: time from the onset of convection up to the explosion; $\rho_{\rm ign}$ and $T_{\rm ign}$: central density and temperature at C-ignition; $\rho_{\rm simm}$ and $T_{\rm simm}$: central density and temperature at the onset of convection; $M(^{12}{\rm C})_{\rm ini}$ and $M(^{12}{\rm C})_{\rm fin}$: amount of ^{12}C available in the accreted structure and that remaining at the explosion; $\Delta M(^{12}{\rm C})$: amount of ^{12}C consumed via nuclear burning up to the explosion; $M^{\rm max}_{\rm conv}$: maximum extension of the convective zone; $M_{\rm exp}$, $\rho_{\rm exp}$, $\eta_{\rm exp}$: mass coordinate where the explosion occurs and the corresponding values of density and neutronization there; $v_{\rm exp}$: maximum convective velocity at the explosion; $\overline{\eta}_{\rm exp}$: neutronization at the explosion averaged over the convective zone; $\eta_{\rm c,0}$: initial value of central neutronization.

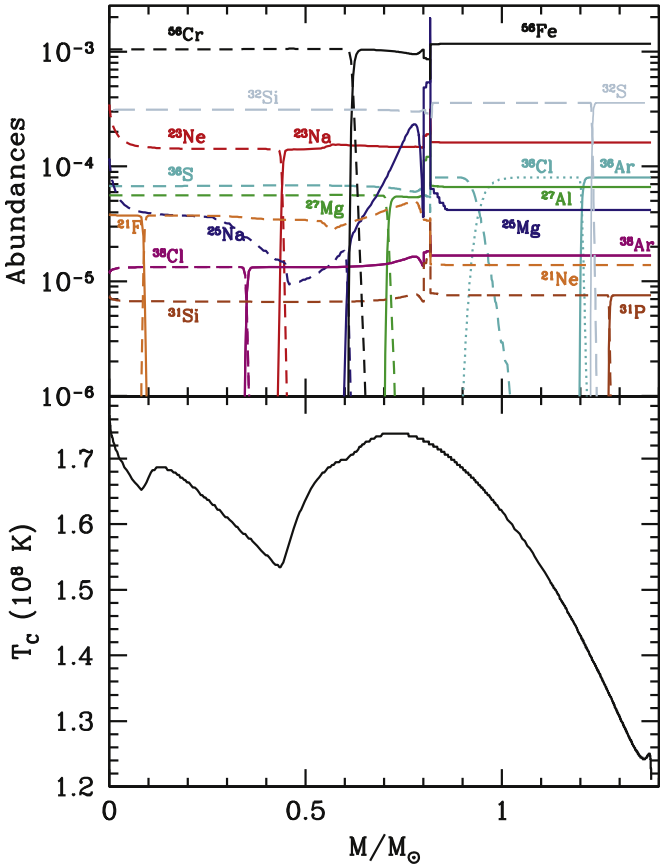

Figure 2. Thermal and chemical structure of the ZSUN model at the beginning of the simmering phase. Isobars belonging to an URCA pair are identified with solid lines (electron-capturing one) and dashed lines (beta-decaying one).

be deposited, density increases along the whole accreting WD and the URCA shell moves outward, cooling a zone progressively larger. On the contrary, due to compressional heating, the whole WD heats up. The interplay between these two processes determines the formation of minima in the temperature profile, as the one at $M \simeq 0.082\ M_\odot$, corresponding to the ^{21}(Ne, F) URCA pair, or that at $M \simeq 0.430\ M_\odot$, corresponding to the ^{23}(Na, Ne) one. The earlier the URCA process activates during the accretion phase, the smaller the traces on the temperature profile at the C-ignition (e.g., the plateau at $M \simeq 0.620\ M_\odot$, corresponding to the ^{25}(Mg, Na) URCA pair). The effects of URCA processes either ignited at the beginning of the accretion or with a small abundance of the ^AZ isobar are smeared off by the compressional heating.

Each jump in the neutronization displayed in the lower panel of Figure 1 is the signature of a given URCA pair and/or double electron-capture triplet. Moreover, the boost in η for $\rho \geqslant 4 \times 10^9$ g cm^{-3} corresponds to the onset of C-burning, via $^{12}{\rm C}(^{12}{\rm C}, {\rm p})^{23}{\rm Na}$, which revives the ^{23}(Na, Ne) URCA pair and activate the other major source of neutronization $^{12}{\rm C}({\rm p}, \gamma)^{13}{\rm N}(e^-, \nu_e)^{13}{\rm C}$. For $\rho \geqslant 5 \times 10^9$ g cm^{-3} convection turns on, neutronized matter is diluted and neutronization increases at a lower rate. Finally, when local heating via C-burning largely dominates over the compressional heating, a large overpressure is determined and the whole structure starts to expand, while neutronization increases substantially.

The dependence of our results on the progenitor metallicity is summarized in Table 2 and illustrated in Figure 3. The ZLOW model is scarcely affected by the URCA shell induced cooling, due to the low initial abundance of isobars ^ZA. Hence, C-ignition occurs at lower density and higher temperature compared to the ZSUN model, causing a smaller increase of neutronization during the simmering phase.

In the ZHIG model, due to the larger initial abundance of isobars ^AZ, the cooling effects of URCA processes are larger compared to the ZSUN model and a larger amount of mass has to be accreted to trigger C-ignition at the center, occurring at very large density (see Table 2). During the simmering phase the central density of the ZHIG model exceeds 7×10^9 g cm^{-3}, thus activating the $^{20}{\rm Ne}(e^-, \nu_e)^{20}{\rm F}$ reaction. Note that at this epoch, due to C-burning, ^{20}Ne abundance has increased from $X(^{20}{\rm Ne})_{\rm ini} = 3.18 \times 10^{-3}$ to $X(^{20}{\rm Ne}) = 4.12 \times 10^{-3}$. Hence, due to efficient neutrino cooling, the innermost region of the WD becomes radiative while the location of maximum temperature shifts outwards (dotted lines in Figure 3). The zones above the maximum temperature location decouples from the innermost region, which evolves at almost constant temperature. When thermal heating via nuclear burning overcomes the compressional heating, the whole structure expands and electron-captures on ^{20}Ne stop. Notwithstanding, the WD center can not heat up because thermal energy flows inwards from the burning region on a timescale definitively larger than the residual evolutionary time up to the explosion.

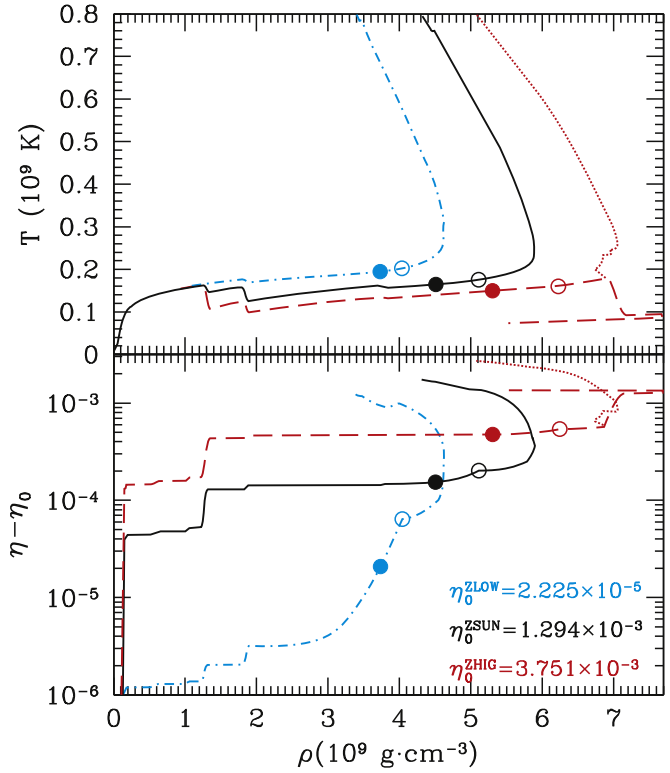

Figure 3. Evolution of the central temperature (upper panel) and neutron excess (lower panel) as a function of the WD central density. Solid, dotted–dashed and dashed lines refer to the ZSUN, ZLOW and ZHIG models, respectively. Dotted lines refer to the mass coordinate where temperature is a maximum in the ZHIG model. Filled and open dots mark the C-ignition and the simmering onset epochs, respectively.

As a matter of fact the explosion occurs off-center, at mass coordinate $M_{\rm exp} \simeq 0.0149\,M_{\odot}$.

4. Conclusions

We have computed the evolution of three accreting WDs from the beginning of the the mass transfer process up to the thermal runaway, through the simmering phase, paying special attention to the treatment of convection and URCA processes. We find that weak processes play a crucial role in determining the physical conditions and neutronization at the explosion. Contrary to the claims by Piro & Bildsten (2008), Chamulak et al. (2008), and Martínez-Rodríguez et al. (2016), we find that the simmering phase acts as an amplifier of the initial metallicity differences, determining quite different neutron excesses, densities and convective velocities at the explosion. The comparison of our models with those present in the extant literature is far from being straightforward, due to the different input physics adopted in the various numerical simulations (e.g., initial WD models, nuclear network, equation of state, nuclear reaction rates, mixing algorithm, etc.), so we will address this issue in a forthcoming paper.

In principle, one could define a final-to-initial neutron-excess relation, that could be used to decode the neutron excesses measured in SNIa explosions or remnants and, then, to deduce the progenitor metallicity. By linearly interpolating the values listed in Table 2 of $\overline{\eta}_{\rm exp}$ as a function of Z for models ZLOW, ZSUN and ZHIG, we obtain

$$\overline{\eta}_{\rm exp} = 1.285\eta_0 + 6.649 \times 10^{-4},$$
$$R^2 = 1.00. \quad (1)$$

By recalling that η_0 depends only on the initial metallicity,

$$\eta_0 = 9.380 \times 10^{-2}\, Z - 4.656 \times 10^{-7}. \quad (2)$$

Equation (1) can be written as

$$\overline{\eta}_{\rm exp} = 1.205 \times 10^{-1}\, Z + 6.643 \times 10^{-4}, \quad (3)$$

and the latter could be inverted to obtain

$$Z = 8.295\overline{\eta}_{\rm exp} - 5.507 \times 10^{-3}. \quad (4)$$

Note that the coefficients in all the previous equations depend on the assumed distribution of metals in the CO WD progenitors.

Badenes et al. (2008) and Park et al. (2013) measured the Mn and Cr mass for the Tycho and *Kepler* remnants and derived $\overline{\eta}_{\rm exp,Tycho} = 4.36 \times 10^{-3}$ and $\overline{\eta}_{\rm exp,\mathit{Kepler}} = 4.55 \times 10^{-3}$. By assuming that these values represent the neutronization at the explosion epoch and that the latter is equal to that of the initial WD, mainly determined by the ^{22}Ne abundance ($\eta_0 = Z/11$), they derived the progenitor metallicity of Tycho's and *Kepler*'s supernova to be $Z_{\rm Tycho} = 0.048 = 3.5\,Z_{\odot}$ and $Z_{\mathit{Kepler}} = 0.050 = 3.6\,Z_{\odot}$, respectively. By using Equation (4), we derive $Z_{\rm Tycho} = 0.0307 = 2.22\,Z_{\odot}$ and $Z_{\mathit{Kepler}} = 0.0322 = 2.34\,Z_{\odot}$, in fairly good agreement with the evidence that stars in the thin disk of the Galaxy have metallicity lower than $3\,Z_{\odot}$.

According to our results, the higher the metallicity, the larger $\overline{\eta}_{\rm exp}$ and $\rho_{\rm exp}$ and, hence, the lower the amount of ^{56}Ni synthesized during the explosion. Hence, low metallicity progenitors are expected to produce brighter SNe Ia. The explosion phase of models discussed here will be presented in a forthcoming paper.

We remark that our results do not apply to SNe Ia progenitor models involving WDs with total mass definitively lower than the Chandrasekar limit.

The variation of $\overline{\eta}$ during the accretion and simmering phases depends mainly on the heavy elements abundance in the WD progenitor. However, the physical properties during the accretion phase depends also on $\dot{M}$ and to lesser extent on the WD initial mass. In particular, for a fixed $M_{\rm WD}$, the lower $\dot{M}$, the larger $M_{\rm acc}$ and the higher $\rho_{\rm ign}$ (e.g., see Piersanti et al. 2003). This should affect the evolution during the simmering phase, producing a spread in $\overline{\eta}_{\rm exp}$ and $\rho_{\rm exp}$.

In this work we ignored the effect of gravitational settling of metals during the WD cooling phase. Since we found that their initial presence affects the evolution of the accreting WD, we plan to investigate the impact of sedimentation on $\overline{\eta}$ during accretion and simmering phases.

L.P., S.C., and O.S. acknowledge founding from the PRIN-MIUR grant 20128PCN59; E.B. and I.D. acknowledge founding from the MINECO-FEDER grant AYA2015-63588-P; G.M.P. is partly supported by the Deutsche Forschungsgemeinschaft through contract SFB 1245.

References

Badenes, C., Bravo, E., & Hughes, J. P. 2008, ApJL, 680, L33
Barkat, Z., & Wheeler, J. C. 1990, ApJ, 355, 602
Bisnovatyi-Kogan, G. S. 2001, MNRAS, 321, 315

Bravo, E., Domínguez, I., Badenes, C., Piersanti, L., & Straniero, O. 2010, ApJL, 711, L66
Bruenn, S. W. 1973, ApJL, 183, L125
Caughlan, G. R., & Fowler, W. A. 1988, ADNDT, 40, 283
Chamulak, D. A., Brown, E. F., Timmes, F. X., & Dupczak, K. 2008, ApJ, 677, 160
Couch, R. G., & Arnett, W. D. 1975, ApJ, 196, 791
Cox, J. P., & Giuli, R. T. 1968, Principles of Stellar Structure (New York: Gordon and Breach)
Cristallo, S., Straniero, O., Gallino, R., et al. 2009, ApJ, 696, 797
Denissenkov, P. A., Truran, J. W., Herwig, F., et al. 2015, MNRAS, 447, 2696
Fuller, G. M., Fowler, W. A., & Newman, M. J. 1985, ApJ, 293, 1
García-Senz, D., & Woosley, S. E. 1995, ApJ, 454, 895
Höflich, P., Gerardy, C., Linder, E., et al. 2003, LNP, 635, 203
Hoyle, F., & Fowler, W. A. 1960, ApJ, 132, 565
Iben, I., Jr. 1978a, ApJ, 219, 213
Iben, I., Jr. 1978b, ApJ, 226, 996
Iben, I., Jr. 1982, ApJ, 253, 248
Iben, I., Jr., & Tutukov, A. V. 1984, ApJS, 54, 335
Langanke, K., & Martínez-Pinedo, G. 2001, ADNDT, 79, 1
Lesaffre, P., Podsiadlowski, P., & Tout, C. A. 2005, MNRAS, 356, 131
Lodders, K. 2003, ApJ, 591, 1220
Martínez-Rodríguez, H., Piro, A. L., Schwab, J., & Badenes, C. 2016, ApJ, 825, 57
Mochkovitch, R. 1996, A&A, 311, 152
Moreno-Raya, M. E., López-Sánchez, Á. R., Mollúa, M., et al. 2016, MNRAS, 462, 1281
Nomoto, K., Thielemann, F.-K., & Yokoi, K. 1984, ApJ, 286, 644
Oda, T., Hino, M., Muto, K., Takahara, M., & Sato, K. 1994, ADNDT, 56, 231
Paczyński, B. 1972, ApL, 11, 53
Park, S., Badenes, C., Mori, K., et al. 2013, ApJL, 767, L10
Piersanti, L., Gagliardi, S., Iben, I., Jr., & Tornambé, A. 2003, ApJ, 583, 885
Piersanti, L., Straniero, O., & Cristallo, S. 2007, A&A, 462, 1051
Piro, A. L., & Bildsten, L. 2008, ApJ, 673, 1009
Stein, J., Barkat, Z., & Wheeler, J. C. 1999, ApJ, 523, 381
Straniero, O., Gallino, R., & Cristallo, S. 2006, NuPhA, 777, 311
Suzuki, T., Toki, H., & Nomoto, K. 2016, ApJ, 817, 163
Timmes, F. X., Brown, E. F., & Truran, J. W. 2003, ApJL, 590, L83
Tsuruta, S., & Cameron, A. G. W. 1970, Ap&SS, 7, 374
Woosley, S. E., & Weaver, T. A. 1986, ARA&A, 24, 205
Wunsch, S., & Woosley, S. E. 2004, ApJ, 616, 1102
Zegers, R. G. T., Brown, E. F., Akimune, H., et al. 2008, PhRvC, 77, 024307